Investigating the Influence of a Viscous Flux Correction for a High-Order k-Exact Discretization Scheme on Unstructured Grids

Florian Setzwein* and Peter Ess†

Institute of Combustion Technology, German Aerospace Center (DLR), Stuttgart, 70569, Germany

Peter Gerlinger‡

IVLR, University of Stuttgart, Stuttgart, 70569, Germany

We present a correction term for the calculation of viscous fluxes both at interior faces and at Dirichlet boundary conditions in the framework of unstructured vertex-centered k-exact finite-volume schemes. The method achieves a higher accuracy for simulations of wall dominated flows and ensures a proper order of accuracy even on distorted unstructured grids. The effect of the correction term is presented in terms of test cases for both laminar and turbulent wall bounded flows. It is demonstrated how the proposed correction term improves the entire solution accuracy, thus pointing out the importance of an accurate discretization of viscous fluxes in the vicinity of walls.

I. Introduction

High-order schemes for unstructured grids offer great capabilities for the reduction of computation time for detailed Large-Eddy Simulations, while maintaining a large geometric flexibility in the mesh generation process.[1] Promising approaches, such as the Discontinuous Galerkin method[2–5] or the spectral volume method[6–9] offer a higher order of accuracy on unstructured grids by introducing additional degrees of freedom within computational elements. Unfortunately, implementing such schemes into established finite-volume flow solvers, which often include many complex models, is not a trivial task and requires a high verification and validation effort. A promising approach to improve unstructured state-of-the-art finite-volume solvers with a higher spatial accuracy is the k-exact multiple-correction approach by Pont et al.[10,11] Its key is a successive correction of approximate Green-Gauss derivatives, which enables a high-order reconstruction with favorable parallel scaling properties and low implementation effort. The original cell-centered method has recently been extended to vertex-centered median-dual grids in combination with an implicit fractional step scheme for the solution of the Navier-Stokes equations.[12] Besides that, a novel central convective flux approximation has been proposed that is based on an adaptive dissipation control, in order to achieve a stable solution with a minimum amount of numerical dissipation and without a tedious search for optimum empirical simulation parameters.[13]

However, the former works did not account for a k-exact treatment of viscous fluxes in the vicinity of wall boundary conditions. Even though the accuracy of viscous fluxes is generally considered less important for the resolution of turbulence, recent work by Chamrathi et al.[14] showed that indeed the viscous flux discretization plays a major role for simulations on marginally resolved grids. In this work, we present a correction term for the calculation of viscous fluxes at both interior element interfaces and and at Dirichlet boundaries, which enables a second order accurate discretization in space. This enhanced accuracy is maintained on

*PhD Student, German Aerospace Center (DLR), Stuttgart, 70569, Germany
†Postdoctoral Fellow, Senior AIAA Member, German Aerospace Center (DLR), Stuttgart, 70569, Germany
‡Professor, IVLR University of Stuttgart, Stuttgart, 70569, Germany

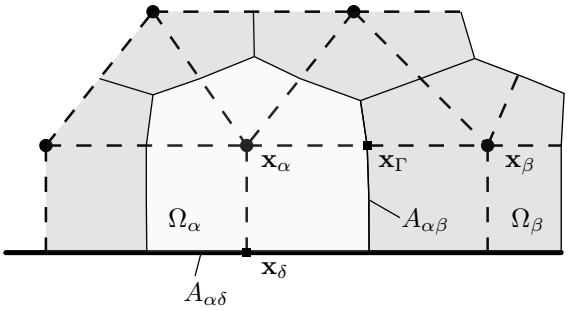

Figure 1: Median-dual grid in 2D, indicated in solid lines. The corresponding primary grid is drawn in dashed lines. The simulation variables are stored at the location of primary grid nodes, e.g. $\mathbf{x}_\alpha$ or $\mathbf{x}_\beta$.

unstructured median-dual grids. The novel flux formulation is applied to the implicit high-order k-exact multiple-correction scheme on vertex-centered grids,[12,15,16] which is implemented in DLR's finite-volume flow solver ThetaCOM (**t**urbulent **he**at release extension for **TA**U in its **com**bustion version). The impact of the viscous flux correction concerning the solution accuracy is examined on both laminar and turbulent wall bounded flow problems, namely a Hagen-Poiseuille flow, a laminar flow around a cylinder and a turbulent pipe flow.

II. Numerical Methods

The following section gives a brief overview of the utilized k-exact multiple-correction approach for vertex-centered grids. Starting point is a general transport equation for a field variable ϕ that is convected in a fluid flow with velocity u_i and subject to diffusive transport with diffusivity D:

$$\frac{\partial \phi}{\partial t} + \frac{\partial}{\partial x_i}\left(u_i \phi\right) + \frac{\partial}{\partial x_i}\left(D \frac{\partial \phi}{\partial x_i}\right) = 0. \tag{1}$$

Equation (1) is solved with a finite-volume approach, where the computational domain Ω is divided into N non-overlapping computational elements Ω_α. These elements are given by the median-dual representation of the tesselated domain. The latter is denoted as primary grid and consists of linear elements such as triangles or quadrilaterals in $2D$ and tetrahedra, hexahedra, prisms or pyramids in $3D$. Figure 1 shows an examplary median-dual representation of a two dimensional grid. Two elements Ω_α and Ω_β are said to be adjacent if they share a common face $A_{\alpha\beta}$. The set $\{\beta_\alpha^{(1)}\}$ is referred to as the first neighborhood of an element Ω_α and it comprises all adjacent elements to it. Elements that are located at the domain boundary also comprise a set of points $\{\delta_\alpha\}$, which will be used to evaluate numerical boundary fluxes. For reasons of clarity, the respective element faces on which these points are located will be denoted by $A_{\alpha\delta}$.

Central to the finite-volume approach is the volume-average $\overline{\phi}_\alpha$ of the considered field variable over Ω_α, which is defined by

$$\overline{\phi}_\alpha = \frac{1}{|\Omega_\alpha|} \iiint_{\Omega_\alpha} \phi(\mathbf{x}) \, \mathrm{d}V. \tag{2}$$

The volume-averaging is applied to the governing equation (1), to obtain a set of equations where the unkown volume-averages $\overline{\phi}_\alpha$ act as degrees of freedom

$$\frac{\partial \overline{\phi}_\alpha}{\partial t} + \frac{1}{|\Omega_\alpha|} \sum_{\beta \in \{\beta_\alpha^{(1)}\}} \left[F_C^{(\alpha\beta)} + F_D^{(\alpha\beta)}\right] + \frac{1}{|\Omega_\alpha|} \sum_{\delta \in \{\delta_\alpha\}} \left[F_C^{(\alpha\delta)} + F_D^{(\alpha\delta)}\right] = 0. \tag{3}$$

Here, the convective and diffusive fluxes are defined for all interior faces by

$$F_C^{(\alpha\beta)} := \iint_{A_{\alpha\beta}} u_i \phi \, n_i \, \mathrm{d}A \qquad \text{and} \qquad F_D^{(\alpha\beta)} := \iint_{A_{\alpha\beta}} D \frac{\partial \phi}{\partial x_i} \, n_i \, \mathrm{d}A \tag{4}$$

and vice versa for fluxes across boundary faces $A_{\alpha\delta}$. The goal of any finite-volume scheme is the approximation of these fluxes in terms of the volume-averages $\overline{\phi}_\alpha$ to close the system of equations and proceed to a

new time step. In this work, we utilize a k-exact reconstruction approach for this task, where the solution in the vicinity of an element Ω_α is locally approximated by a Taylor polynomial $\phi^{(k+1)}(\mathbf{x};\mathbf{x}_\alpha)$ of degree k:

$$\phi^{(k+1)}(\mathbf{x};\mathbf{x}_\alpha) = \phi\Big|_{\mathbf{x}_\alpha}^{(k+1)} + \frac{\partial\phi}{\partial x_{i_1}}\bigg|_{\mathbf{x}_\alpha}^{(k)} (x_{i_1} - x_{i_1,\alpha}) + \ldots + \frac{1}{k!}\,\frac{\partial^k\phi}{\partial x_{i_1}\ldots\partial x_{i_k}}\bigg|_{\mathbf{x}_\alpha}^{(1)} (x_{i_1} - x_{i_1,\alpha})\ldots(x_{i_k} - x_{i_k,\alpha})\,. \quad (5)$$

The point $\mathbf{x}_\alpha$ marks a vertex of the underlying primary grid structure, around which the median-dual element Ω_α is constructed and at which the volume-average $\overline{\phi}_\alpha$ is stored. The value $\phi|_{\mathbf{x}_\alpha}^{(k+1)}$ denotes the approximation of the point value $\phi(\mathbf{x}_\alpha)$ with an accuracy of $\mathcal{O}(h^{k+1})$. In a similar fashion, the n^{th} derivative term refers to an approximation of the true point-valued derivative of ϕ at $\mathbf{x}_\alpha$ with an accuracy of $\mathcal{O}(h^{k-n+1})$. The k-exact reconstruction approach aims to determine these unknown polynomial coefficients in such a way that the respective accuracy levels are maintained irrespective of the underling grid structure. Besides that, it is also required that the volume-average (2) of the reconstruction polynomial (5) is satisified on a compact neighborhood of elements around Ω_α.[17] By using the k-exact multiple-correction approach,[10,12] the unknown derivatives are approximated with a Green-Gauss algorithm that does not meet the aforementioned accuracy constraints in the first place. The derivatives are then successively corrected to higher orders of accuracy through geometric correction matrices, that solely depend on the numerical grid. In this way, the data for enhancing the order of accuracy is implicitly transferred through derivatives of adjacent elements. This is a major benefit of this approach, since it is not required to exchange large element stencils on domain boundaries, which is generally the case for non-local k-exact finite-volume schemes. As a result, the multiple-correction approach significantly reduces the implementation effort for a high-order reconstruction and guarantees good parallelization properties. Thus, it is an excellent tool to improve state-of-the-art finite-volume solvers towards a higher spatial accuracy. For a detailed overview of the applied method we refer to our prior work.[12,13,15,16]

Once the reconstruction polynomials are calculated, they are used to approximate the surface integrals of transport equation (1) to close the system of equations. In this work, the approximation of the numerical fluxes $F_C^{(\alpha\beta)}$ and $F_D^{(\alpha\beta)}$ is realized with a single-point integration, that is based on a Taylor series expansion around a point $\mathbf{x}_\Gamma$ located on the surface $A_{\alpha\beta}$:

$$\iint_{A_{\alpha\beta}} f_i\, n_i \,\mathrm{d}A = f_i\Big|_{\mathbf{x}_\Gamma} \mathcal{S}_i^{(\alpha\beta)} + \frac{\partial f_i}{\partial x_{j_1}}\bigg|_{\mathbf{x}_\Gamma} \mathcal{S}_{i,j_1}^{(\alpha\beta,\Gamma)} + \ldots + \frac{1}{k!}\,\frac{\partial^k f_i}{\partial x_{j_1}\ldots\partial x_{j_k}}\bigg|_{\mathbf{x}_\Gamma} \mathcal{S}_{i,j_1\ldots j_k}^{(\alpha\beta,\Gamma)} + \mathcal{O}\left(h^{k+1}\right). \quad (6)$$

In this way, any flux function f_i can be integrated by means of the reconstructed point value $\phi|_{\mathbf{x}_\Gamma}$ and its derivatives at $\mathbf{x}_\Gamma$, as long as these point values maintain appropriate orders of accuracies. The integration method is based on the introduction of rank p geometric surface moments, which ensure a proper integration of the surface-integral in a single point, regardless of the shape of the surface $A_{\alpha\beta}$. They are generally defined as

$$\mathcal{S}_{i,j_1 j_2\ldots j_p}^{(\alpha\beta,\Gamma)} = \iint_{A_{\alpha\beta}} n_i\,(x_{j_1} - x_{j_1,\Gamma})\,(x_{j_2} - x_{j_2,\Gamma})\ldots\left(x_{j_p} - x_{j_p,\Gamma}\right)\,\mathrm{d}A, \quad (7)$$

where the subscripts i and j_p are separated by a comma, to highlight that i indicates the face normal direction and j_p the spatial direction of the terms $\left(x_{j_p} - x_{j_p,\Gamma}\right)$. The superscripts $(\alpha\beta,\Gamma)$ indicate the elements Ω_α and Ω_β adjacent to the face, as well as the point $\mathbf{x}_\Gamma$ where the Taylor series expansion is located. The rank zero surface moment $\mathcal{S}_i^{(\alpha\beta)}$ does not include the superscript Γ since it only refers to the joint normal of the face $A_{\alpha\beta}$ and is thus independent of $\mathbf{x}_\Gamma$. The same surface moment definition holds also for faces $A_{\alpha\delta}$ located at domain boundaries.

The approximation of convective fluxes $f_i = u_i\phi$ is based on a novel central discretization approach with an adaptive numerical dissipation control. It ensures the stability of the scheme while the numerical dissipation is reduced to a minimum. This greatly enhances the simulation results compared to conventional discretization schemes for convective fluxes, regardless of empirical flow parameters. The approach has been described in detail in our recent work.[13] In the following, we will focus on how to utilize the given integration method for the approximation of viscous fluxes $f_i = D\,(\partial\phi/\partial x_i)$ in both the interior of the domain and at Dirichlet boundaries. The former has already been described in a prior work,[12] but in a slightly different form. Thus, the methodology presented here should give an enhanced geometric interpretation of the scheme and also leads to the foundation for the extension to the viscous flux approximation at boundary faces.

A. Viscous fluxes at interior faces

The following derivations are presented for a 2-exact reconstruction. Starting point for the calculation of viscous fluxes at interior faces is the insertion of the flux function $f_i = D\,(\partial\phi/\partial x_i)$ into Equation (6), which gives

$$F_D^{(\alpha\beta)} = D\,\frac{\partial\phi}{\partial x_i}\bigg|_{\mathbf{x}_\Gamma} \mathcal{S}_i^{(\alpha\beta)} + D\,\frac{\partial^2\phi}{\partial x_i \partial x_j}\bigg|_{\mathbf{x}_\Gamma} \mathcal{S}_{i,j}^{(\alpha\beta,\Gamma)} + |A_{\alpha\beta}|\,\mathcal{O}\left(h^2\right). \tag{8}$$

We start by expressing the gradient $\partial\phi/\partial x_i|_{\mathbf{x}_\Gamma}$ at the surface $A_{\alpha\beta}$ in terms of the reconstruction polynomial of the adjacent elements Ω_α and Ω_β. It is desireable to do this in terms of the volume-averages $\overline{\phi}_\alpha$ and $\overline{\phi}_\beta$ to obtain a stronger coupling of the underlying linear system of equations and a resulting suppression of parasitic errors. This is also the main idea of the discretization scheme by Mathur and Murthy,[18] that will be extended for the approximation of Equation (8) in the context of a k-exact reconstruction. It is also referred to as face-tangent scheme[19–21] and is based on the work of Muzaferija and Gosman[22] and Demirdžić and Muzaferija,[23] which are also frequently used to discretize viscous fluxes on unstructured grids.[24] All these schemes rely on the separation of the scalar product between the gradient and the surface normal $(\partial\phi/\partial x_i|_{\mathbf{x}_\Gamma})\mathcal{S}_i^{(\alpha\beta)}$ into an orhogonal and a non-orthogonal part[25]

$$\frac{\partial\phi}{\partial x_i}\bigg|_{\mathbf{x}_\Gamma} \mathcal{S}_i^{(\alpha\beta)} = \underbrace{\varepsilon^{(\alpha\beta)}\,\frac{\partial\phi}{\partial x_i}\bigg|_{\mathbf{x}_\Gamma} \Delta x_i{}^{(\alpha\beta)}}_{\text{orthogonal}} + \underbrace{\varepsilon^{(\alpha\beta)}\,\frac{\partial\phi}{\partial x_i}\bigg|_{\mathbf{x}_\Gamma} \Delta\tilde{x}_i^{(\alpha\beta)}}_{\text{non-orthogonal}}, \tag{9}$$

with the distance vectors $\Delta x_i{}^{(\alpha\beta)} := x_{i,\beta} - x_{i,\alpha}$ and $\Delta\tilde{x}_i^{(\alpha\beta)} := \mathcal{S}_i^{(\alpha\beta)}/\varepsilon^{(\alpha\beta)} - \Delta x_i{}^{(\alpha\beta)}$. The geometric quantity $\varepsilon^{(\alpha\beta)}$ places a degree of freedom for the construction of the scheme and can be used to unify the different approaches by Muzaferija and Gosman,[22] Demirdžić and Muzaferija[23] or Mathur and Murthy.[18] An overview of these different approaches can be found in the work of Jasak.[25] However, for the present work, the parameter is calculated according to the Mathur-Murthy scheme:

$$\varepsilon^{(\alpha\beta)} = \frac{\mathcal{S}_i^{(\alpha\beta)}\mathcal{S}_i^{(\alpha\beta)}}{\Delta x_j{}^{(\alpha\beta)}\,\mathcal{S}_j^{(\alpha\beta)}}. \tag{10}$$

This formulation is also known as over-relaxed approach[25] and leads to a stronger weighting of the non-orthogonal part when the surface normal $\mathcal{S}_i^{(\alpha\beta)}$ and the distance vector $\Delta x_i{}^{(\alpha\beta)}$ are not aligned. This relationship is shown in Figure 2.

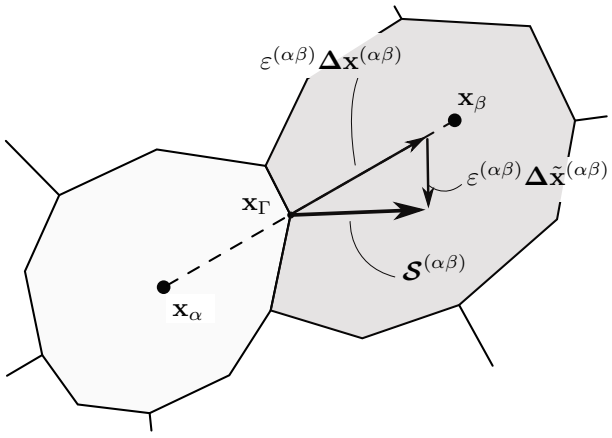

Figure 2: Splitting of the surface normal $\boldsymbol{\mathcal{S}}^{\alpha\beta}$ into a part $\varepsilon^{(\alpha\beta)}\mathbf{\Delta x}^{(\alpha\beta)}$ that is projected onto $\mathbf{\Delta x}^{(\alpha\beta)}$ and a part $\varepsilon^{(\alpha\beta)}\mathbf{\Delta\tilde{x}}^{(\alpha\beta)}$ orthogonal to it.

Our target is to approximate the scalar products $(\partial\phi/\partial x_i|_{\mathbf{x}_\Gamma})\Delta x_i{}^{(\alpha\beta)}$ and $(\partial\phi/\partial x_i|_{\mathbf{x}_\Gamma})\Delta\tilde{x}_i^{(\alpha\beta)}$ in terms of the reconstruction polynomials of the adjacent elements Ω_α and Ω_β, while preserving the underlying k-exact conservation of the mean.[12] For this, a Taylor series expansion is constructed around point $\mathbf{x}_\Gamma$, which is

located at the face $A_{\alpha\beta}$. For $k = 2$ this leads to the following reconstruction polynomial

$$\phi(\mathbf{x}) = \phi\Big|_{\mathbf{x}_\Gamma} + \frac{\partial\phi}{\partial x_i}\bigg|_{\mathbf{x}_\Gamma}(x_i - x_{i,\Gamma}) + \frac{1}{2}\frac{\partial^2\phi}{\partial x_i \partial x_j}\bigg|_{\mathbf{x}_\Gamma}(x_i - x_{i,\Gamma})(x_j - x_{j,\Gamma}) + \mathcal{O}\left(h^3\right). \tag{11}$$

Equation (11) is volume-averaged over the adjacent elements Ω_α and Ω_β, which results in the following relations:

$$\overline{\phi}_\alpha = \phi\Big|_{\mathbf{x}_\Gamma} + \frac{\partial\phi}{\partial x_i}\bigg|_{\mathbf{x}_\Gamma}\mathcal{M}_i^{(\alpha,\Gamma)} + \frac{1}{2}\frac{\partial^2\phi}{\partial x_i \partial x_j}\bigg|_{\mathbf{x}_\Gamma}\mathcal{M}_{ij}^{(\alpha,\Gamma)} + \mathcal{O}\left(h^3\right), \tag{12a}$$

$$\overline{\phi}_\beta = \phi\Big|_{\mathbf{x}_\Gamma} + \frac{\partial\phi}{\partial x_i}\bigg|_{\mathbf{x}_\Gamma}\mathcal{M}_i^{(\beta,\Gamma)} + \frac{1}{2}\frac{\partial^2\phi}{\partial x_i \partial x_j}\bigg|_{\mathbf{x}_\Gamma}\mathcal{M}_{ij}^{(\beta,\Gamma)} + \mathcal{O}\left(h^3\right). \tag{12b}$$

These relations are based on the geometric volume moments $\mathcal{M}_{i_1 i_2 \ldots i_R}^{(\beta,\alpha)}$ of rank R, which can be calculated in a similar way to the surface moments

$$\mathcal{M}_{i_1 i_2 \ldots i_R}^{(\beta,\alpha)} = \frac{1}{|\Omega_\beta|}\iiint_{\Omega_\beta}(x_{i_1} - x_{i_1,\alpha})(x_{i_2} - x_{i_2,\alpha})\ldots(x_{i_R} - x_{i_R,\alpha})\,\mathrm{d}V. \tag{13}$$

The first superscript β refers to the element Ω_β on which the averaging takes place and the second superscript α denotes a point $\mathbf{x}_\alpha$, that is used to center the moment. Note, that both superscripts are separated by a comma to highlight their different meaning. Volume moments where the centering point coincides with the primary grid node of the element to be integrated are denoted by $\mathcal{M}_{i_1 i_2 \ldots i_R,\alpha} := \mathcal{M}_{i_1 i_2 \ldots i_R}^{(\alpha,\alpha)}$. These are actually the only volume-moments to be stored in memory, since the integration over other points can be obtained from binomial relations,[26,27] as for example by

$$\mathcal{M}_i^{(\beta,\alpha)} = \mathcal{M}_{i,\beta} + \Delta x_i{}^{(\alpha\beta)}, \tag{14a}$$

$$\mathcal{M}_{ij}^{(\beta,\alpha)} = \mathcal{M}_{ij,\beta} + \Delta x_i{}^{(\alpha\beta)}\mathcal{M}_{j,\beta} + \Delta x_j{}^{(\alpha\beta)}\mathcal{M}_{i,\beta} + \Delta x_i{}^{(\alpha\beta)}\Delta x_j{}^{(\alpha\beta)}. \tag{14b}$$

Equations (12a) and (12b) are now subtracted from each other, in order to express the projection of the gradient $(\partial\phi/\partial x_i|_{\mathbf{x}_\Gamma})$ onto the distance vector $\Delta x_i{}^{(\alpha\beta)}$ in terms of

$$\frac{\partial\phi}{\partial x_i}\bigg|_{\mathbf{x}_\Gamma}\Delta x_i{}^{(\alpha\beta)} = \left(\overline{\phi}_\beta - \overline{\phi}_\alpha\right) - \frac{\partial\phi}{\partial x_i}\bigg|_{\mathbf{x}_\Gamma}\Delta\mathcal{M}_i^{(\alpha\beta)} - \frac{1}{2}\frac{\partial^2\phi}{\partial x_i \partial x_j}\bigg|_{\mathbf{x}_\Gamma}\Delta\mathcal{M}_{ij}^{(\alpha\beta)} + \mathcal{O}\left(h^3\right). \tag{15}$$

This relation can be used to approximate the orthogonal part of Equation (9), where the following terms are introduced for reason of clarity

$$\Delta\mathcal{M}_i^{(\alpha\beta)} := \mathcal{M}_{i,\beta} - \mathcal{M}_{i,\alpha} \tag{16a}$$

$$\Delta\mathcal{M}_{ij}^{(\alpha\beta)} := \underbrace{\mathcal{M}_{ij,\beta} - \mathcal{M}_{ij,\alpha} + \frac{1}{2}\Delta x_i{}^{(\alpha\beta)}\left(\mathcal{M}_{j,\beta} + \mathcal{M}_{j,\alpha}\right) + \frac{1}{2}\Delta x_j{}^{(\alpha\beta)}\left(\mathcal{M}_{i,\beta} + \mathcal{M}_{i,\alpha}\right)}_{=\mathcal{M}_{ij}^{(\beta,\Gamma)} - \mathcal{M}_{ij}^{(\alpha,\Gamma)}}. \tag{16b}$$

The derivatives $\partial\phi/\partial x_i|_{\mathbf{x}_\Gamma}$ and $\partial^2\phi/(\partial x_i \partial x_j)|_{x_\Gamma}$ on the right of Equation (15) are approximated centrally from the reconstruction polynomials of both adjacent elements:

$$\begin{aligned}
\frac{\partial\phi}{\partial x_i}\bigg|_{\mathbf{x}_\Gamma} &= \frac{1}{2}\left(\frac{\partial}{\partial x_i}\phi^{(3)}(\mathbf{x}_\Gamma;\mathbf{x}_\alpha) + \frac{\partial}{\partial x_i}\phi^{(3)}(\mathbf{x}_\Gamma;\mathbf{x}_\beta)\right) + \mathcal{O}\left(h^2\right), \\
\frac{\partial^2\phi}{\partial x_i \partial x_j}\bigg|_{\mathbf{x}_\Gamma} &= \frac{1}{2}\left(\frac{\partial^2}{\partial x_i \partial x_j}\phi^{(3)}(\mathbf{x}_\Gamma;\mathbf{x}_\alpha) + \frac{\partial^2}{\partial x_i \partial x_j}\phi^{(3)}(\mathbf{x}_\Gamma;\mathbf{x}_\beta)\right) + \mathcal{O}\left(h\right).
\end{aligned} \tag{17}$$

Since the terms $\Delta\mathcal{M}_i^{(\alpha\beta)}$ and $\Delta\mathcal{M}_{ij}^{(\alpha\beta)}$ scale with $\mathcal{O}(h^2)$ and $\mathcal{O}(h)$, respectively, a third-order accuracy is preserved for the approximation of $(\partial\phi/\partial x_i|_{\mathbf{x}_\Gamma})\Delta x_i{}^{(\alpha\beta)}$ when a 2-exact reconstruction is conducted.

It remains to approximate the non-orthogonal term of Equation (9). To do this, we evaluate the k-exact Taylor polynomial from Equation (11) at point $\tilde{x}_{i,\Gamma} = x_{i,\Gamma} + \Delta\tilde{x}_i^{(\alpha\beta)}$ and solve for the scalar product $\partial\phi/\partial x_i|_{\mathbf{x}_\Gamma}\Delta\tilde{x}_i^{(\alpha\beta)}$. This results in the following relation:

$$\left.\frac{\partial\phi}{\partial x_i}\right|_{\mathbf{x}_\Gamma}\Delta\tilde{x}_i^{(\alpha\beta)} = \left(\phi(\tilde{\mathbf{x}}_\Gamma) - \left.\phi\right|_{\mathbf{x}_\Gamma}\right) - \frac{1}{2}\left.\frac{\partial^2\phi}{\partial x_i\partial x_j}\right|_{\mathbf{x}_\Gamma}\Delta\tilde{x}_i^{(\alpha\beta)}\Delta\tilde{x}_j^{(\alpha\beta)} + \mathcal{O}\left(h^3\right). \tag{18}$$

On fully orthogonal grids, both points $x_{i,\Gamma}$ and $\tilde{x}_{i,\Gamma}$ coincide, which causes this equation to vanish. It now remains to approximate the unknown point-values of ϕ at $\mathbf{x}_\Gamma$ and $\tilde{\mathbf{x}}_\Gamma$ with respective orders of accuracies. This can be achieved by evaluating the reconstruction polynomials of both adjacent elements Ω_α and Ω_β at $\mathbf{x}_\Gamma$ and by performing a central averaging. For $k = 2$, this leads to

$$\phi(\tilde{\mathbf{x}}_\Gamma) = \frac{1}{2}\left(\phi^{(3)}(\tilde{\mathbf{x}}_\Gamma;\mathbf{x}_\alpha) + \phi^{(3)}(\tilde{\mathbf{x}}_\Gamma;\mathbf{x}_\beta)\right) + \mathcal{O}\left(h^3\right), \tag{19a}$$

$$\left.\phi\right|_{\mathbf{x}_\Gamma} = \frac{1}{2}\left(\phi^{(3)}(\mathbf{x}_\Gamma;\mathbf{x}_\alpha) + \phi^{(3)}(\mathbf{x}_\Gamma;\mathbf{x}_\beta)\right) + \mathcal{O}\left(h^3\right). \tag{19b}$$

A central approach is also used to approximate the second derivative at $\mathbf{x}_\Gamma$, as it was already done in Equation (17). Finally, all terms are inserted into the viscous flux in Equation (8), which then can be cast into the following form:

$$F_D^{(\alpha\beta)} = F_{D,LO}^{(\alpha\beta)} + F_{D,STAB}^{(\alpha\beta)} + F_{D,HO}^{(\alpha\beta)} + |A_{\alpha\beta}|\,\mathcal{O}\left(h^2\right). \tag{20}$$

The terms $F_{D,LO}^{(\alpha\beta)}$ and $F_{D,STAB}^{(\alpha\beta)}$ are also present in the original Mathur-Murthy scheme[18] and are defined by

$$F_{D,LO}^{(\alpha\beta)} = D\,\varepsilon^{(\alpha\beta)}\left(\overline{\phi}_\beta - \overline{\phi}_\alpha\right), \tag{21a}$$

$$F_{D,STAB}^{(\alpha\beta)} = \frac{1}{2}D\,\varepsilon^{(\alpha\beta)}\left(\left.\frac{\partial\phi}{\partial x_i}\right|_{\mathbf{x}_\alpha}^{(2)} + \left.\frac{\partial\phi}{\partial x_i}\right|_{\mathbf{x}_\beta}^{(2)}\right)\Delta\tilde{x}_i^{(\alpha\beta)}. \tag{21b}$$

They are often calculated with a deferred-correction[28] approach, where the former term $F_{D,LO}^{(\alpha\beta)}$ is treated implicitly and the latter term $F_{D,STAB}^{(\alpha\beta)}$ explicitly.[22,24] This results in a higher diagonal dominance of the system matrix and thus a higher robustness of the scheme.[25] The term $F_{D,HO}^{(\alpha\beta)}$ acts as a correction for the scheme to satisfy the k-exact conservation. It is defined by

$$\begin{aligned}
F_{D,HO}^{(\alpha\beta)} = {} & -\tfrac{1}{2}D\varepsilon^{(\alpha\beta)}\left(\left.\tfrac{\partial\phi}{\partial x_i}\right|_{\mathbf{x}_\alpha}^{(2)} + \left.\tfrac{\partial\phi}{\partial x_i}\right|_{\mathbf{x}_\beta}^{(2)}\right)\Delta\mathcal{M}_i^{(\alpha\beta)} \quad \Big\} \text{1-exact contribution} \\
& -\tfrac{1}{4}D\varepsilon^{(\alpha\beta)}\left(\left.\tfrac{\partial^2\phi}{\partial x_i\partial x_j}\right|_{\mathbf{x}_\alpha}^{(1)} + \left.\tfrac{\partial^2\phi}{\partial x_i\partial x_j}\right|_{\mathbf{x}_\beta}^{(1)}\right)\left(\Delta\mathcal{M}_{ij}^{(\alpha\beta)} - \tfrac{2}{\varepsilon^{(\alpha\beta)}}\mathcal{S}_{i,j}^{(\alpha\beta,\Gamma)}\right) \\
& +\tfrac{1}{8}D\varepsilon^{(\alpha\beta)}\left(\left.\tfrac{\partial^2\phi}{\partial x_i\partial x_j}\right|_{\mathbf{x}_\beta}^{(1)} - \left.\tfrac{\partial^2\phi}{\partial x_i\partial x_j}\right|_{\mathbf{x}_\alpha}^{(1)}\right)\left[\Delta {x_i}^{(\alpha\beta)}\left(\Delta\mathcal{M}_j^{(\alpha\beta)} - \Delta\tilde{x}_j^{(\alpha\beta)}\right)\right] \\
& +\tfrac{1}{8}D\varepsilon^{(\alpha\beta)}\left(\left.\tfrac{\partial^2\phi}{\partial x_i\partial x_j}\right|_{\mathbf{x}_\beta}^{(1)} - \left.\tfrac{\partial^2\phi}{\partial x_i\partial x_j}\right|_{\mathbf{x}_\alpha}^{(1)}\right)\left[\Delta {x_j}^{(\alpha\beta)}\left(\Delta\mathcal{M}_i^{(\alpha\beta)} - \Delta\tilde{x}_i^{(\alpha\beta)}\right)\right]. \quad \Big\} \text{2-exact contribution}
\end{aligned} \tag{22}$$

This expression also contains the product between the Hessian $\partial^2\phi/(\partial x_i\partial x_j)|_{x_\Gamma}$ and the first surface moment $\mathcal{S}_{i,j}^{(\alpha\beta,\Gamma)}$ required to approximate the surface integral in Equation (8) with a higher order of accuracy.

B. Viscous fluxes at Dirichlet boundaries

In the following, the discretization approach for viscous fluxes given above will be extended for element faces located at Dirichlet boundaries of the computational domain. An extension to Neumann boundary conditions is straight forward, since the respective fluxes can be inserted directly into Equation (8). However, if Dirichlet boundary conditions are used, the derivative at the surface must be approximated from the imposed boundary

values. To maintain the k-exact conservation properties, this requires a similar correction as for the interior fluxes. Starting point is the viscous flux of the scalar ϕ over the boundary face $A_{\alpha\delta}$, which is discretized by

$$F_D^{(\alpha\delta)} = D \left.\frac{\partial \phi}{\partial x_i}\right|_{\mathbf{x}_\delta} \mathcal{S}_i^{(\alpha\delta)} + |A_{\alpha\beta}| \, \mathcal{O}\left(h\right). \tag{23}$$

In contrast to the internal fluxes, we omit rank one surface moments $\mathcal{S}_{i,j}^{(\alpha\delta,\delta)}$ for the surface integration, since they exhibit much smaller values than interior moments $\mathcal{S}_{i,j}^{(\alpha\beta,\Gamma)}$. The justification for this negligence will also become evident from the results in section III. In analogy to Equation (9), the flux is separated into an orthogonal and a non-orthogonal part

$$\left.\frac{\partial \phi}{\partial x_i}\right|_{\mathbf{x}_\delta} \mathcal{S}_i^{(\alpha\delta)} = \varepsilon^{(\alpha\delta)} \left.\frac{\partial \phi}{\partial x_i}\right|_{\mathbf{x}_\delta} \Delta {x_i}^{(\alpha\delta)} + \varepsilon^{(\alpha\delta)} \left.\frac{\partial \phi}{\partial x_i}\right|_{\mathbf{x}_\delta} \Delta \tilde{x}_i^{(\alpha\delta)}, \tag{24}$$

where we introduce the distance vectors $\Delta {x_i}^{(\alpha\delta)} = x_{i,\delta} - x_{i,\alpha}$ and $\Delta \tilde{x}_i^{(\alpha\delta)} = \mathcal{S}_i^{(\alpha\delta)} / \varepsilon^{(\alpha\delta)} - \Delta {x_i}^{(\alpha\delta)}$. The parameter $\varepsilon^{(\alpha\delta)}$ is calculated in a similar fashion as for the interior fluxes given in Equation (10). The orthogonal part requires the product $\partial\phi/\partial x_i|_{\mathbf{x}_\delta} \Delta {x_i}^{(\alpha\delta)}$ to be approximated. For $k = 2$, this is achieved with a Taylor series expansion around the point $\mathbf{x}_\delta$ which is located on the surface $A_{\alpha\delta}$. The resulting polynomial is then used to approximate the point value $\phi\Big|_{\mathbf{x}_\alpha}$ and its gradient $\left.\frac{\partial \phi}{\partial x_i}\right|_{\mathbf{x}_\alpha}$ at the primary grid node $\mathbf{x}_\alpha$ of the boundary element:

$$\phi\Big|_{\mathbf{x}_\alpha} = \phi\Big|_{\mathbf{x}_\delta} - \left.\frac{\partial \phi}{\partial x_i}\right|_{\mathbf{x}_\delta} \Delta {x_i}^{(\alpha\delta)} + \frac{1}{2} \left.\frac{\partial^2 \phi}{\partial x_i \partial x_j}\right|_{\mathbf{x}_\delta} \Delta {x_i}^{(\alpha\delta)} \Delta {x_j}^{(\alpha\delta)} + \mathcal{O}\left(h^3\right), \tag{25a}$$

$$\left.\frac{\partial \phi}{\partial x_i}\right|_{\mathbf{x}_\alpha} = \left.\frac{\partial \phi}{\partial x_i}\right|_{\mathbf{x}_\delta} - \left.\frac{\partial^2 \phi}{\partial x_i \partial x_j}\right|_{\mathbf{x}_\delta} \Delta {x_j}^{(\alpha\delta)} + \mathcal{O}\left(h^2\right), \tag{25b}$$

The insertion of Equation (25b) into (25a) reveals the product $\partial\phi/\partial x_i|_{\mathbf{x}_\delta} \Delta {x_i}^{(\alpha\delta)}$ in terms of

$$\left.\frac{\partial \phi}{\partial x_i}\right|_{\mathbf{x}_\delta} \Delta {x_i}^{(\alpha\delta)} = 2 \left(\phi\Big|_{\mathbf{x}_\delta} - \phi\Big|_{\mathbf{x}_\alpha} \right) - \left.\frac{\partial \phi}{\partial x_i}\right|_{\mathbf{x}_\alpha} \Delta {x_i}^{(\alpha\delta)} + \mathcal{O}\left(h^3\right). \tag{26}$$

It is worth mentioning that the point value $\phi|_{\mathbf{x}_\delta}$ is given by the boundary condition and, hence, is known. In theory, the remaining values at point $\mathbf{x}_\alpha$ could be determined by the reconstruction polynomial of the element Ω_α. But unfortunately, this approach did not result in a stable scheme in preliminary numerical experiments. Instead, it is required to also express the product $(\partial\phi/\partial x_i|_{\mathbf{x}_\alpha}) \Delta {x_i}^{(\alpha\delta)}$ by means of both point values $\phi|_{\mathbf{x}_\delta}$ and $\phi|_{\mathbf{x}_\alpha}$, which results in a stronger coupling of the underlying system of equations. To do this, we construct a second Taylor series expansion around node $\mathbf{x}_\alpha$

$$\phi\Big|_{\mathbf{x}_\delta} = \phi\Big|_{\mathbf{x}_\alpha} + \left.\frac{\partial \phi}{\partial x_i}\right|_{\mathbf{x}_\alpha} \Delta {x_i}^{(\alpha\delta)} + \frac{1}{2} \left.\frac{\partial^2 \phi}{\partial x_i \partial x_j}\right|_{\mathbf{x}_\alpha} \Delta {x_i}^{(\alpha\delta)} \Delta {x_j}^{(\alpha\delta)} + \mathcal{O}\left(h^3\right), \tag{27}$$

which can be rearranged to yield the following formulation for the product $(\partial\phi/\partial x_i|_{\mathbf{x}_\alpha}) \Delta {x_i}^{(\alpha\delta)}$

$$\left.\frac{\partial \phi}{\partial x_i}\right|_{\mathbf{x}_\alpha} \Delta {x_i}^{(\alpha\delta)} = \phi\Big|_{\mathbf{x}_\delta} - \phi\Big|_{\mathbf{x}_\alpha} + \frac{1}{2} \left.\frac{\partial^2 \phi}{\partial x_i \partial x_j}\right|_{\mathbf{x}_\alpha} \Delta {x_i}^{(\alpha\delta)} \Delta {x_j}^{(\alpha\delta)} + \mathcal{O}\left(h^3\right). \tag{28}$$

This expression is finally inserted into Equation (26).

To compute the non-orthogonal part $(\partial\phi/\partial x_i|_{\mathbf{x}_\delta}) \Delta \tilde{x}_i^{(\alpha\delta)}$ in Equation (24), we extrapolate the gradient at surface $A_{\alpha\delta}$ from the interior of element Ω_α and multiply it with the orthogonal distance vector $\Delta \tilde{x}_i^{(\alpha\delta)}$:

$$\left.\frac{\partial \phi}{\partial x_i}\right|_{\mathbf{x}_\delta} \Delta \tilde{x}_i^{(\alpha\delta)} = \left(\left.\frac{\partial \phi}{\partial x_i}\right|_{\mathbf{x}_\alpha} + \left.\frac{\partial^2 \phi}{\partial x_i \partial x_j}\right|_{\mathbf{x}_\alpha} \Delta {x_j}^{(\alpha\delta)} \right) \Delta \tilde{x}_i^{(\alpha\delta)} + \mathcal{O}\left(h^2\right). \tag{29}$$

Finally, inserting Equation (26) and (29) into Equation (24) and replacing the analytic derivatives by their k-exact approximative counterparts gives the following expression for the scalar product $(\partial\phi/\partial x_i|_{\mathbf{x}_\delta})\mathcal{S}_i^{(\alpha\delta)}$. For $k = 2$, this results in:

$$\begin{aligned}\left.\frac{\partial\phi}{\partial x_i}\right|_{\mathbf{x}_\delta}\mathcal{S}_i^{(\alpha\delta)} &= \varepsilon^{(\alpha\delta)}\left(\phi\Big|_{\mathbf{x}_\delta} - \phi\Big|_{\mathbf{x}_\alpha}^{(3)} + \frac{1}{2}\frac{\partial^2\phi}{\partial x_i\partial x_j}\Big|_{\mathbf{x}_\alpha}^{(1)}\Delta x_i{}^{(\alpha\delta)}\Delta x_j{}^{(\alpha\delta)}\right)\\ &+ \varepsilon^{(\alpha\delta)}\left(\left.\frac{\partial\phi}{\partial x_i}\right|_{\mathbf{x}_\alpha}^{(2)} + \frac{\partial^2\phi}{\partial x_i\partial x_j}\Big|_{\mathbf{x}_\alpha}^{(1)}\Delta x_j{}^{(\alpha\delta)}\right)\Delta\tilde{x}_i^{(\alpha\delta)} + |A_{\alpha\beta}|\,\mathcal{O}\left(h^2\right),\end{aligned} \tag{30}$$

where the point-value $\phi|_{\mathbf{x}_\alpha}^{(3)}$ is calculated from the volume-averaged reconstruction polynomial of element Ω_α

$$\phi\Big|_{\mathbf{x}_\alpha}^{(3)} = \overline{\phi}_\alpha - \left.\frac{\partial\phi}{\partial x_i}\right|_{\mathbf{x}_\alpha}^{(2)}\mathcal{M}_{i,\alpha} - \frac{1}{2}\frac{\partial^2\phi}{\partial x_i\partial x_j}\Big|_{\mathbf{x}_\alpha}^{(1)}\mathcal{M}_{ij,\alpha}. \tag{31}$$

Similarly to interior faces, we can decompose the final k-exact viscous fluxes at Dirichlet boundary faces into the following three terms:

$$F_D^{(\alpha\delta)} = F_{D,LO}^{(\alpha\delta)} + F_{D,STAB}^{(\alpha\delta)} + F_{D,HO}^{(\alpha\delta)} + |A_{\alpha\beta}|\,\mathcal{O}\left(h\right). \tag{32}$$

The first two terms $F_{D,LO}^{(\alpha\delta)}$ and $F_{D,STAB}^{(\alpha\delta)}$ act as counterparts to the Mathur-Murthy scheme of the interior fluxes and are defined by

$$F_{D,LO}^{(\alpha\delta)} = D\,\varepsilon^{(\alpha\delta)}\left(\phi\Big|_{\mathbf{x}_\delta} - \overline{\phi}_\alpha\right) \tag{33a}$$

$$F_{D,STAB}^{(\alpha\delta)} = D\,\varepsilon^{(\alpha\delta)}\left.\frac{\partial\phi}{\partial x_i}\right|_{\mathbf{x}_\alpha}^{(2)}\Delta\widetilde{x}_i^{(\delta\alpha)}. \tag{33b}$$

Likewise, the term $F_{D,HO}^{(\alpha\delta)}$ acts as a higher-order correction to achieve the k-exact constraints along the boundary

$$F_{D,HO}^{(\alpha\delta)} = \underbrace{D\,\varepsilon^{(\alpha\delta)}\left.\frac{\partial\phi}{\partial x_i}\right|_{\mathbf{x}_\alpha}^{(2)}\mathcal{M}_{i,\alpha}}_{\text{1-exact contribution}} + \underbrace{\frac{1}{2}D\,\varepsilon^{(\alpha\delta)}\frac{\partial^2\phi}{\partial x_i\partial x_j}\Big|_{\mathbf{x}_\alpha}^{(1)}\left[\mathcal{M}_{ij,\alpha} + \Delta x_i{}^{(\alpha\delta)}\left(\Delta x_j{}^{(\alpha\delta)} + 2\Delta\widetilde{x}_j^{(\delta\alpha)}\right)\right]}_{\text{2-exact contribution}}. \tag{34}$$

III. Results

In this section, we will investigate the influence of the propsed viscous flux correction terms $F_{D,HO}^{(\alpha\beta)}$ and $F_{D,HO}^{(\alpha\delta)}$ on the overall solution accuracy for both laminar and turbulent wall bounded flows. The considered test cases require the numerical solution to the incompressible Navier-Stokes equations

$$\frac{\partial u_i}{\partial x_i} = 0, \tag{35a}$$

$$\frac{\partial u_i}{\partial t} + \frac{\partial}{\partial x_j}\left(u_i u_j\right) - \nu\frac{\partial^2 u_i}{\partial x_j\partial x_j} = -\frac{1}{\rho}\frac{\partial p}{\partial x_i}, \tag{35b}$$

with the fluid velocity $\mathbf{u}$, the pressure p and the kinematic viscosity ν. This is achieved with a fractional step scheme that requires the implicit solution of a Poisson equation for pressure-velocity coupling, which is second-order accurate in time. The utilization of this method in conjunction with a k-exact reconstruction was shown recently in our work,[12,13] to which we refer for the sake of clarity. The scheme is implemented in DLR's **ThetaCOM** code, which features a multigrid preconditioning for the Poisson equation and an efficient matrix-free Krylov solver for the system of linear equations. All test cases are simulated with a 1- and a 2-exact reconstruction approach, where the convective fluxes are approximed with second- and a

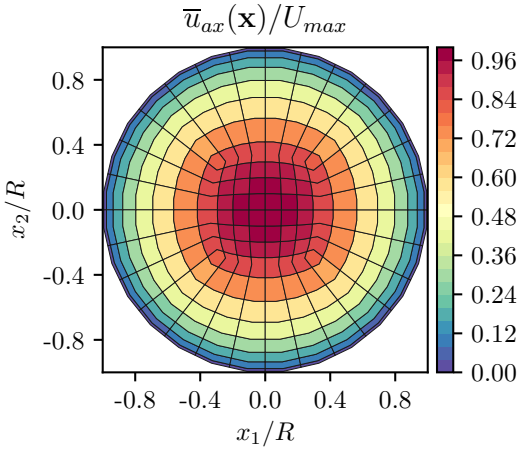

Figure 3: Normalized axial velocity field for the Hagen-Poiseuille flow and a considered grid for the numerical simulation with a mean grid width $h^+ = 1.63$ and 390 median-dual elements.

third-order accuracy, respectively. Besides that, we utilize the central convective flux discretization approach from our recent work,[13] which minimizes the introduced amount of numerical dissipation to a minimum. In all simulations the proposed viscous flux correction is both activated and deactivated, in order to analyze their contribution on the overall solution accuracy.

A. Hagen-Poiseuille Flow

For the first test case, we consider a pipe of radius R with an applied axial pressure gradient G, such that a parabolic laminar flow profile emerges. The solution of this problem is given analytically by the following normalized velocity profile[29]

$$u^+ = \frac{U_{\max}}{u_\tau}\left[1 - \left(\frac{r^+}{\mathrm{Re}_\tau}\right)^2\right], \tag{36}$$

with the radial coordinate $r^+ = \sqrt{x_1^2 + x_2^2}/\delta_\nu$, the normalized center velocity $U_{\max} = GR^2/(4\mu)$ and the shear Reynolds number $\mathrm{Re}_\tau = \rho u_\tau R/\mu$. The variables u_τ and δ_ν refer to the shear velocity and the wall length scale. The parameters are chosen to $G = 0.48\,\mathrm{Pa/m}$, $\mu = 0.01\,\mathrm{Pa\cdot s}$, $\rho = 1.0\,\mathrm{kg/m^3}$ and $R = 0.5\,\mathrm{m}$, which gives $Re_\tau \approx 173$, $\delta_\nu \approx 2.886\,\mathrm{mm}$ and $u_\tau \approx 3.464\,\mathrm{m/s}$. Several simulations are conducted where the pipe cross section is discretized as shown by the median-dual representation in Figure 3. We apply a no-slip wall condition at the outer boundary of the pipe, whereas a periodic boundary condition is applied in the axial direction. In this way it is possible to compute the problem with only two element layers in the axial direction, which significantly reduces the computational effort. Several grid refinement levels are utilized, which are given in Table 1. For all simulations, the flow field is initialized with $\mathbf{u} = 0$ and the axial pressure gradient is applied to the momentum equations as a source term, thus leading to the emergence of a steady laminar flow profile. The latter is obtained by solving the time-dependent Navier-Stokes equations with sufficiently small CFL numbers ≈ 0.05 in order to reduce the influence of temporal discretization errors.

Figure 4 shows the normalized volume-averaged velocity profiles that are calculated with both schemes and a mean grid width $h^+ = 1.63$, which refers to the second grid in Table 1. It can be observed that the viscous correction terms enhance the accuracy of the simulated profiles for both discretization schemes, even though the increase in accuracy is greater for the 2-exact scheme. This result is supported by the L^2-norm of the volume-averaged flow field, which is calculated via the exact solution $\overline{u}^{\mathrm{ex}}_{\mathrm{ax},\alpha}$ by

$$E_{L^2}\left(\overline{u}_{\mathrm{ax}}\right) = \left[\frac{\sum_{\alpha=1}^{N}\left(\overline{u}_{\mathrm{ax},\alpha} - \overline{u}^{\mathrm{ex}}_{\mathrm{ax},\alpha}\right)^2 |\Omega_\alpha|}{\sum_{\alpha=1}^{N}|\Omega_\alpha|}\right]^{1/2}. \tag{37}$$

Figure 5 shows the errors calculated on the various grids given in Table 1 for both the volume-averaged axial velocity $E_{L^2}\left(\overline{u}_{\mathrm{ax}}\right)$, as well as for the axial velocity gradient $E_{L^2}\left(\partial u_{ax}/\partial x_1\right)$. The red curves refer to the

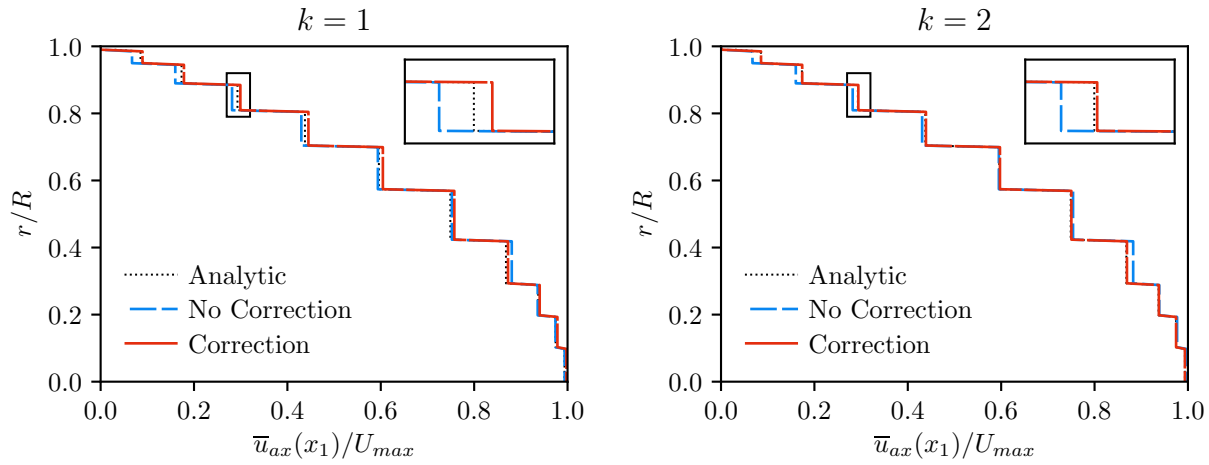

Figure 4: Normalized axial flow profiles for the Hagen-Poiseuille test case, calculated with a mean grid width $h^+ = 1.63$, 390 median-dual elements and for both 1- and 2-exact schemes.

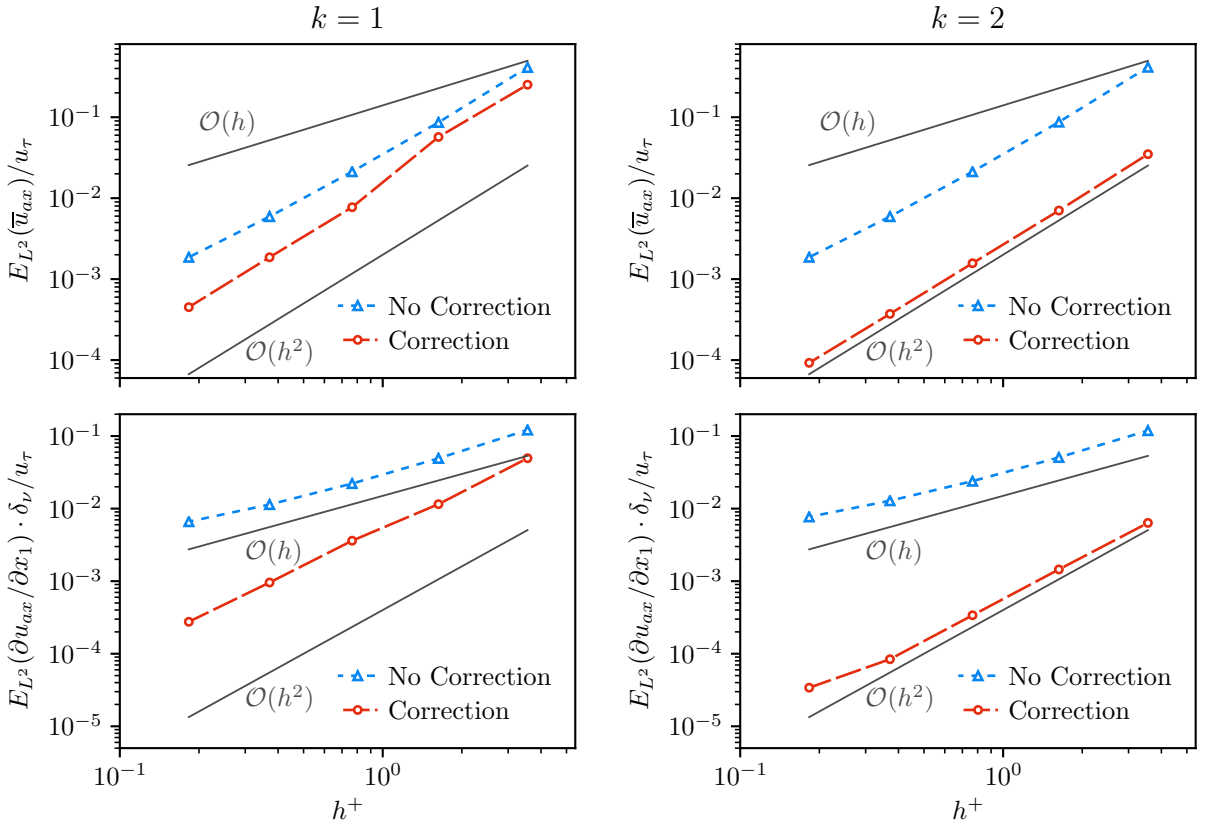

Figure 5: Grid convergence study for the L^2-error of the volume-averaged axial velocity $\overline{u}_{\mathrm{ax}}$ and for the axial velocity gradient $\partial u_{\mathrm{ax}}/\partial x_1|_{\mathbf{x}_\alpha}$ of the Hagen-Poiseuille flow, calculated for both 1- and 2-exact schemes.

Table 1: Gird properties for the Hagen-Poiseuille flow. Given are the number of nodes N in the x_1-x_2-plane, the radial and tangential grid widths $h^+_{\mathrm{rad},1}$ und $h^+_{\mathrm{tan},1}$ as well as the mean grid width h^+ along the entire radius.

Grid	N	$h^+_{\mathrm{rad},1}$	$h^+_{\mathrm{tan},1}$	h^+
1	78	1.79	9.07	3.55
2	390	0.57	3.89	1.63
3	1734	0.24	1.81	0.76
4	7302	0.12	0.88	0.37
5	29958	0.06	0.43	0.18

simulation results where the viscous flux correction terms $F^{(\alpha\beta)}_{D,HO}$ and $F^{(\alpha\delta)}_{D,HO}$ are applied, whereas the blue curves correspond to the default discretization scheme. For both $k = 1$ and $k = 2$, the viscous flux correction significantly increases the overall accuracy levels and leads to a pure second-order accurate convergence of $E_{L^2}(\overline{u}_{\mathrm{ax}})$. The latter implies for the 2-exact scheme that the error convergence of its third-order accurate convective operator is deteriorated by the second-order accurate diffusive operator. This is probably related to the fact, that the error terms of the viscous fluxes dominate over the convective fluxes due to the low Reynolds number of the flow. However, the overall error is reduced by at least one order of magnitude due to the application of the viscous flux correction. It can also be observed, that the errors of the solution gradients collapse to a first-order accuracy when no flux-correction is used, whereas otherwise it features a second-order accuracy. However, for the corrected 2-exact scheme the second-order accuracy of $E_{L^2}(\partial u_{ax}/\partial x_1)$ reduces to $\mathcal{O}(h)$ as the curve falls below a certain threshold of $h^+ \approx 3 \cdot 10^{-1}$. This can be explained by the fact that the gradient approximation is based on volume-averages that exhibit an error of $\mathcal{O}(h^2)$. This error is cascaded in the gradient approximation and manifests itself with $\mathcal{O}(h)$ in the gradient field. However, the resulting first-order error term is comparatively small and only appears below the aforementioned threshold.

B. Laminar Cylinder Flow

This test case been propsed by Schäfer et al.[30] in the workshop "*Flow Simulation with High-Performance Computers*". It has already been used in a prior work[12] to verify the accuracy properties of the proposed k-exact reconstruction scheme, but with a reduced reconstruction order in boundary elements due to stability reasons. Furthermore, no clear distinction was made between the contributions of convective and diffusive flux corrections on the solution accuracy. These issues will be addressed in the following by examining the influence of the viscous correction terms on the solution similarly to the previous test case. The flow of an incompressible fluid around a cylindrical obstacle of diameter $D = 0.1\,\mathrm{m}$ within a channel of size $2.2\,\mathrm{m} \times 0.41\,\mathrm{m}$ at Reynolds number of $\mathrm{Re} = 100$ is conducted. The latter is based on the cylinder's diameter. The obstacle experiences a periodic change in drag and lift force as a result of the downstream vortex shedding. The aim of the simulations is to predict the resulting maxima in the cylinder's drag and lift coefficients, as well as the frequency f of these oscillations. The latter is characterized by the Strouhal number $\mathrm{St} = Df/U$ which is based on cylinder diameter D and the mean flow velocity $U = 1.0\,\mathrm{m/s}$. For a detailed overview of the test case we refer to the work by Schäfer et al.[30] The simulation is conducted on five meshes with varying numbers of

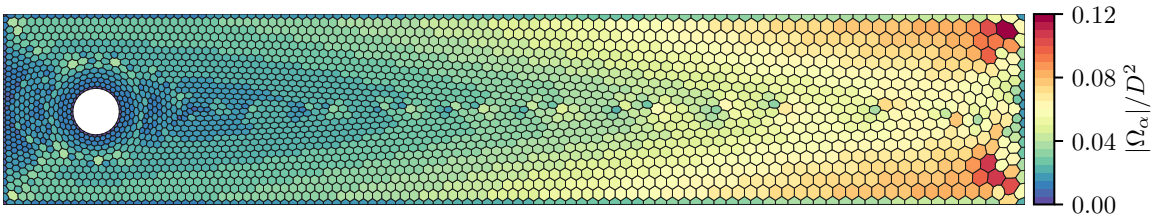

Figure 6: Median-dual grid for the laminar cylinder flow problem with 2753 elements, colored by the normalized element size $|\Omega_\alpha|/D^2$.

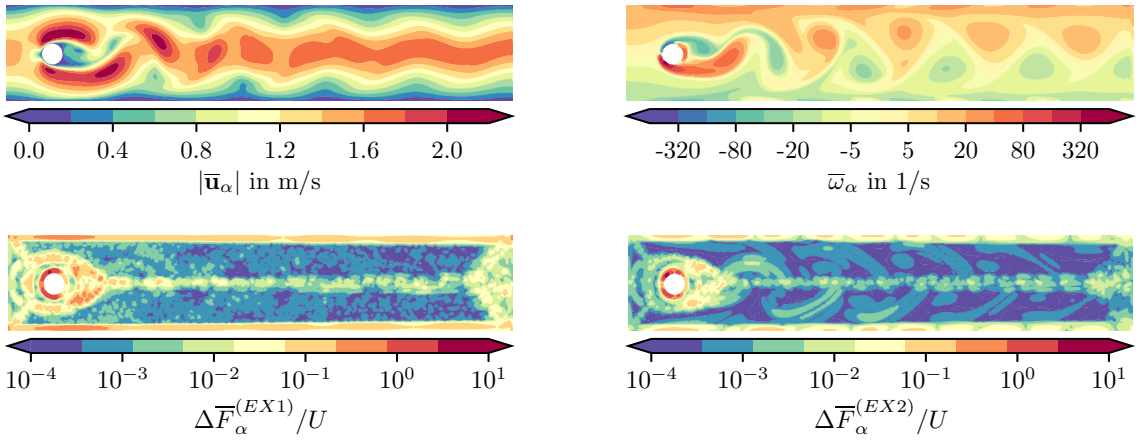

Figure 7: Contours for the laminar cylinder flow problem with 10887 vertices, calculated with the 2-exact scheme and with the applied viscous flux correction. The top figures show the absolute volume-averaged velocity $|\overline{\mathbf{u}}_\alpha|$ as well as the vorticity $\overline{\omega}_\alpha$. The figures below show the contribution from the 1- and 2-exact viscous flux correction that is calculated according to Equation (38).

primary grid vertices $N = \{2753, 5583, 10887, 22152, 43332\}$. The meshes consist of triangular elements and, apart from the cylinder curvature, there is no significant refinement of the elements in the vicinity of walls. The coarsest mesh is shown in Figure 6 by means of its median-dual representation. At the beginning of a simulation run, the velocity field is initialized with $\mathbf{u} = 0$. Subsequently the time-dependent Navier-Stokes equations (35a)-(35b) are solved for a simulation time of 8 s with a Courant-number of approximately 0.4.

Figure 7 shows the calculated flow field that stems from the 2-exact scheme on a grid with 10887 primary grid vertices during the state of maximum lift and with the utilization of the viscous flux correction. The top figures show the absolute velocity and the vorticity. Both fields clearly indicate a Karman vortex street that is in excellent agreement with the solution given in other works.[31–33] The two figures below show the contribution $\Delta\overline{F}_\alpha$ that stems from the k-exact viscous flux correction summed over all element surfaces:

$$\Delta\overline{F}_\alpha = \frac{\Delta t}{|\Omega_\alpha|}\left(\sum_{\beta\in\{\beta_\alpha^{(1)}\}} F_{D,HO}^{(\alpha\beta)}(u_1) + \sum_{\delta\in\{\delta_\alpha\}} F_{D,HO}^{(\alpha\delta)}(u_1)\right). \tag{38}$$

The values are based on the x_1-velocity and are calculated with the respective 1- and 2-exact contributions indicated in Equations (22) and (34). Both correction components are mainly persistent in the vicinity of boundary elements, especially close to the cylinder. A comparison with the mesh structure in Figure 6 indicates that the 1-exact correction is also active in areas where the elements share higher irregularities due to local refinement. In contrast, the 2-exact correction is more affected by the underlying solution, which is revealed by comparison to the vorticity field.

The actual influence of the viscous correction terms on the target variables of this test case is shown in Figure 8 by means of a grid convergence study for both 1- and 2-exact schemes. The blue curves represent calculated values for the Strouhal number St, the maximum lift coefficient $C_{L,max}$ and the maximum drag coefficient $C_{D,max}$ which stem from simulations without the usage of the viscous correction. The red curves, on the other hand, refer to simulations where the terms are used with their corresponding 1- and 2-exact contribution. For both $k = 1$ and $k = 2$, the correction yields more accurate target values at coarser grid levels. This is particularly evident for the 2-exact scheme, where both maximum lift and drag coefficients are approximated with a reasonable accuracy at $N = 10887$ nodes. On the other hand, omitting the viscous flux correction causes the maximum drag coefficient to converge towards too low values. This indicates that it is necessary to maintain the underlying k-exact reconstruction for both convective and diffusive fluxes in order to achieve accurate simulation results. In contrast, an accurate prediction of the Strouhal number is less affected by the correction terms.

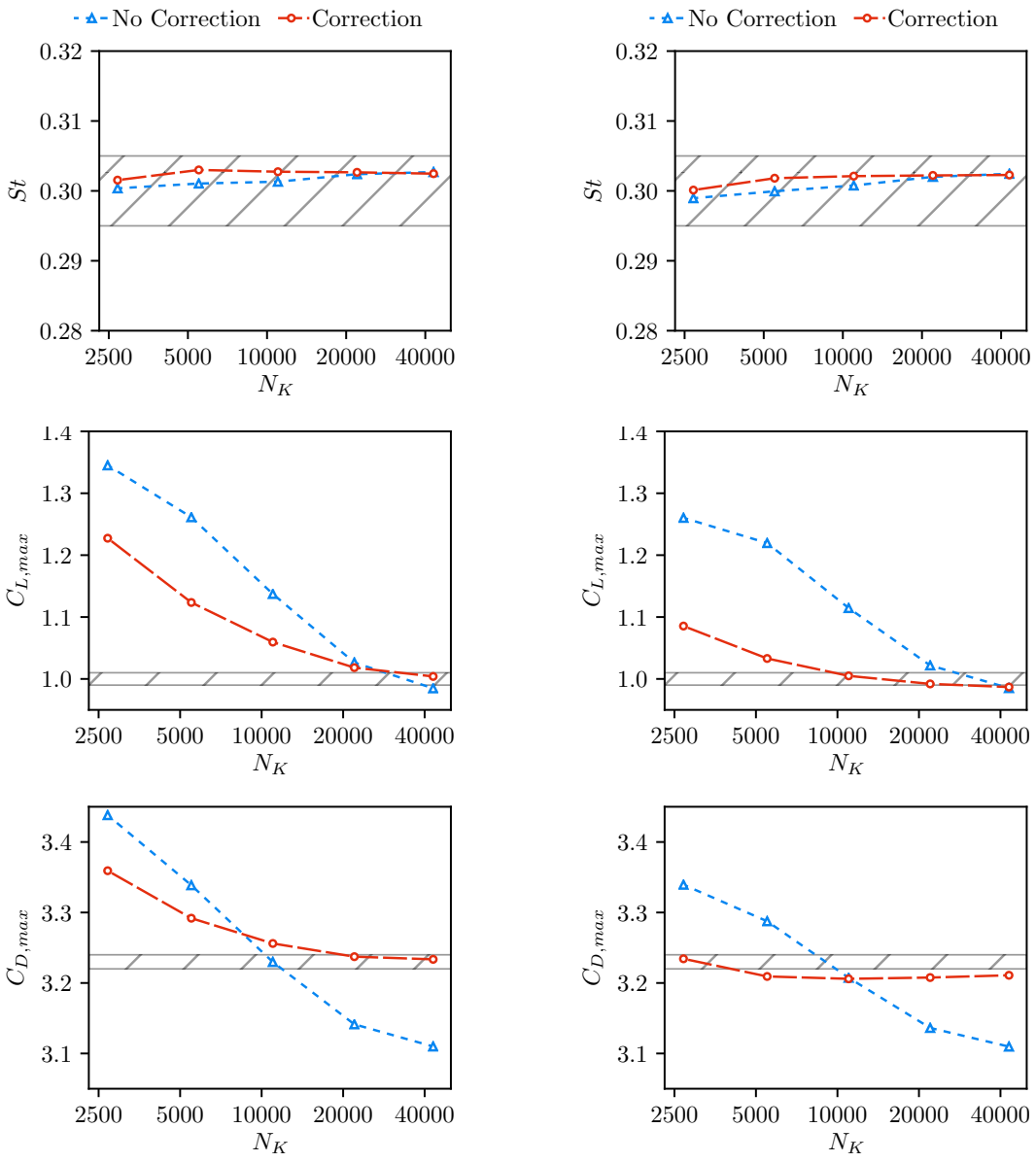

(a) $k = 1$. (b) $k = 2$.

Figure 8: Grid convergence study results for the Strouhal number St, the maximum lift coefficient $C_{L,max}$ and the maximum drag coefficient $C_{D,max}$ of the laminar cylinder test case. The dashed areas correspond to reference values given by Schäfer et al.[30]

C. Turbulent Pipe Flow

This test case is used to simulation a turbulent pipe flow at a Reynolds number $\mathrm{Re}_\tau = u_\tau R/\nu = 180$. The latter is based on the pipe's radius $R = 0.5\,\mathrm{m}$ and the shear stress velocity $u_\tau = 3.6\,\mathrm{m/s}$. The length of the considered pipe is $10R$, periodic boundary conditions are imposed on both ends and no-slip boundary conditions are applied to the pipe walls. The flow is driven by an axial pressure gradient which compensates friction losses and thus yields a constant bulk velocity. For a detailed description of this test case we refer to the work of Eggels et al.[34] and Fukagata and Kasagi.[35] Direct numerical simulation results of Fukagata and Kasagi are used to validate the present simulation outcomes. The flow field is calculated via Large-Eddy Simulations (LES) by solving the spatially filtered, time-dependent Navier-Stokes equations.

Table 2: Grid properties for the turbulent pipe flow test case. N_i refers to the number of nodes in axial, radial and tangential direction and h_i^+ denotes the dimensionless grid scale at the wall.

	N_K	N_{rad}	N_{tan}	N_{ax}	h_{rad}^+	h_{tan}^+	h_{ax}^+
Coarse / Hexas	54665	21	48	64	2.45	23.54	28.13
Coarse / Hybrid	62725	13	62	64	2.20	18.24	28.13
Fine / Hexas	496521	45	104	128	1.13	10.88	14.06
Fine / Hybrid	256839	19	89	128	1.06	12.71	14.06
Reference DNS[35]		96	128	256	0.46	8.54	6.79

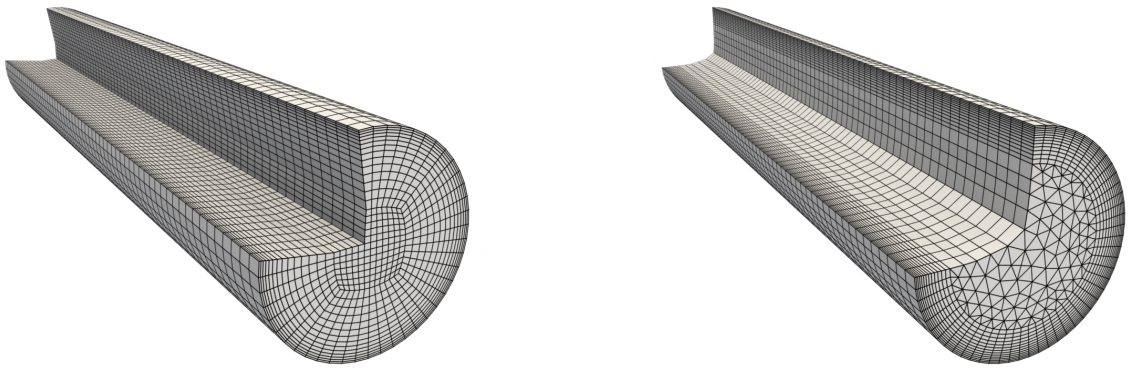

(a) Hexahedral mesh type.

(b) Hybrid mesh type.

Figure 9: Considered mesh types for the turbulent pipe flow test case.

Subgrid-scale modeling is conducted via the Wall-Adapting Local Eddy-Viscosity (WALE) model.[36,37] For a detailed overview on the underlying LES setup, we refer to our previous work.[13] There it was shown, that an accurate prediction of the flow's velocity profiles requires a low amount of numerical dissipation, which in our case is preserved due to the employed adaptive dissipation control. However, the influence of the discretized viscous fluxes on the solution accuracy was not studied in detail, which will be done in the following. We consider two different grid types, namely a purely hexahedral mesh and a hybrid mesh. The latter consists both of prisms in the core region with $r/R < 0.7$ and of hexahedrals in the vicinity of the wall. For both types, a coarse and a fine configuration is utilized, whose particular properties are given in Table 2. Figure 9 shows both coarse grid types. The simulations are initialized with a fully turbulent flow field that stems from preliminary simulations. After an initialization period of 30 flow through times, the flow is temporally averaged for further 250 flow through times in order to gather temporal statistics of the velocity field. These comprise mean values $\langle u_i \rangle$ and mean fluctutations $\langle u_i' u_i' \rangle$.

Figure 10 shows the mean axial flow profiles $\langle u_{ax} \rangle$ that have been calculated on all grids and with both k-exact discretization schemes. Again, the blue lines refer to simulations without the viscous flux correction and the red lines vice versa. At first sight, both schemes feature a very good agreement with the DNS results of Fukagata and Kasagi.[35] Only for the coarse hexahedral grid, the mean axial velocity is slightly overpredicted in the log-law region ($y^+ > 30$). Neglecting the proposed viscous flux correction causes only small deviations in the flow profiles. Mainly on the coarser grids, a slight underestimation of the axial velocity can be observed in the viscous sublayer near the wall. This error is consistent with the results of the Hagen-Poiseuille flow, where the axial velocity was also slightly too low in the absence of the correction term. It thus seems that the correction term mainly affects the regions in which the viscous forces actually dominate the flow, whereas the remaining flow is mainly influenced by the accuracy of the convective operator. Only for the 2-exact scheme and the coarse hexahedral grid the viscous flux correction leads also to a better agreement with the DNS profiles in the log-law region. A slightly higher influence of the viscous flux correction term can be observed in the profiles of the averaged axial velocity fluctuation in Figure 11. Again, all profiles are

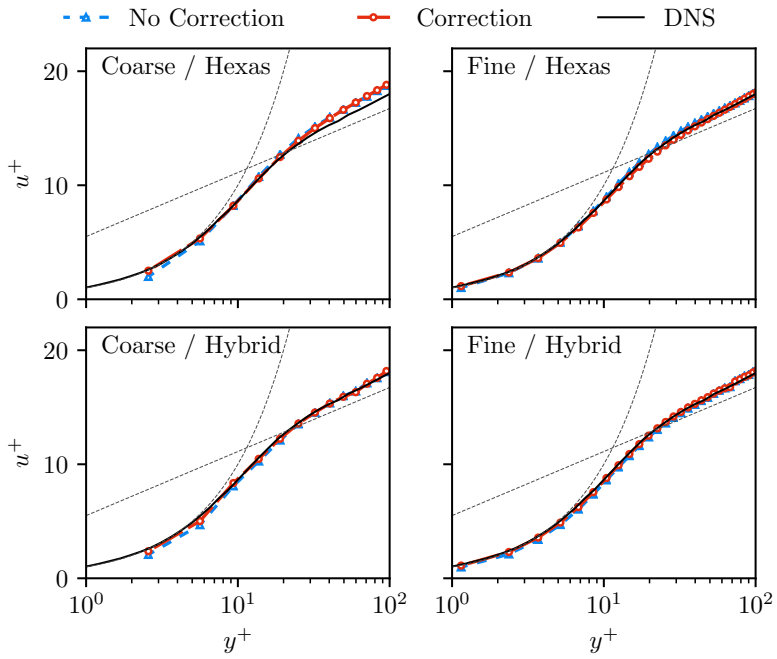

(a) $k = 1$.

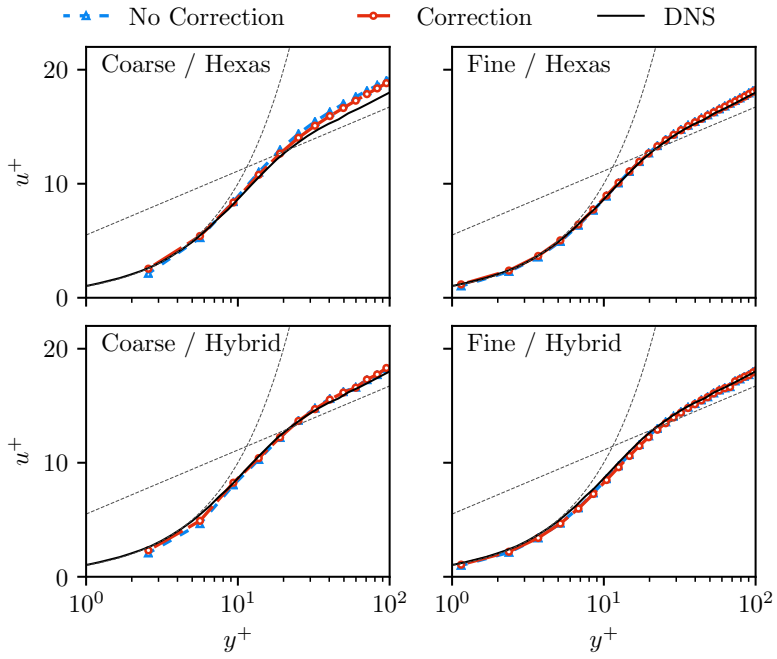

(b) $k = 2$.

Figure 10: Normalized averaged axial velocity profiles $u+ = \langle u_{ax} \rangle / u_\tau$ along the dimensionless wall coordinate $y^+ = y u_\tau / \nu$ for the turbulent pipe flow. The results stem from the four grids given in Table 2. The dashed lines denote the universal law of the wall $u^+ = y^+$ and the logarithmic law of the wall $u^+ = 5.5 + \ln y^+ / 0.41$. The DNS profile stems from the work of Fukagata and Kasagi.[35]

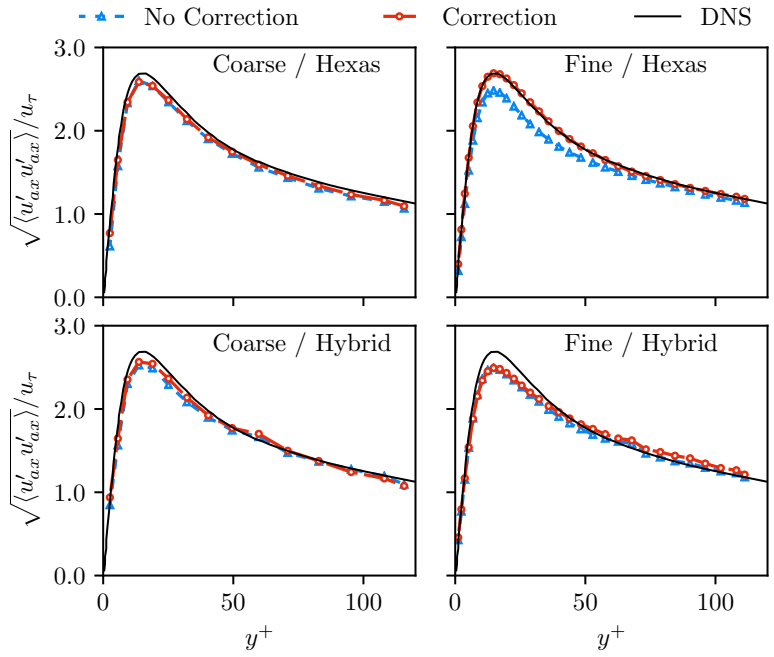

(a) $k = 1$.

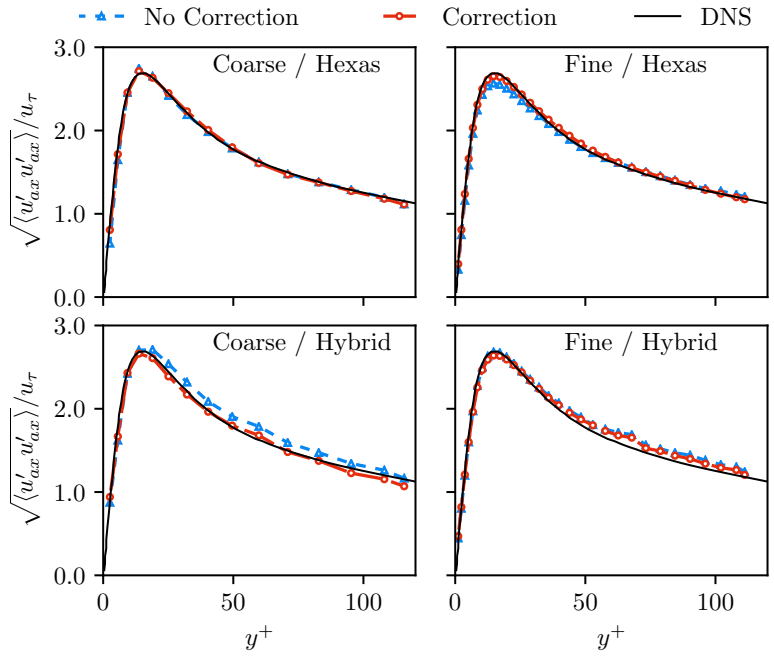

(b) $k = 2$.

Figure 11: Normalized averaged axial velocity fluctuation profiles $\sqrt{\langle u'_{ax} u'_{ax} \rangle}$ against the dimensionless wall coordinate $y^+ = y u_\tau / \nu$ for the turbulent pipe flow. The results stem from the four grids given in Table 2.

in very good agreement to the reference data. For $k = 1$, the utilization of the flux correction leads to a significant improvement of the profile accuracy on the fine hexahedral grid. A similar behaviour is visible for $k = 2$ on both the fine hexahedral grid and on the coarse hybrid grid. Similar discrepancies were also observed for the radial and tangential fluctuations, which are not shown. The results thus indicate that the correction term is required to accurately capture the averaged velocity fluctuation profiles. However, the influence on the solution is considerably weaker than it was for the laminar test cases. In addition, the different grid configurations of the pipe's core seem to have only a relatively small effect on the quality of the flow profiles, regardless of whether the viscous flux correction is used or not.

IV. Conclusion

In this work, we proposed a correction term for the approximation of viscous fluxes both at interior faces and at Dirichlet boundaries in the scope of k-exact schemes on unstructured median-dual grids. The approach has been incorporated into the k-exact multiple-correction method for vertex-centered grids of the DLR in-house code ThetaCOM. The influence of the correction term on the spatial accuracy has been demonstrated for a Hagen-Poiseuille flow, a laminar flow around a cylinder and for a turbulent pipe flow. The results clearly show that the correction significantly improves the overall accuracy for both a 1- and 2-exact discretization scheme.

However, it appeared that its influence on the overall simulation accuracy was higher for the laminar test cases. One possible explanation is that the grids used for the turbulent pipe flow exhibited fewer irregularities than the grids used for the laminar cylinder flow. The viscous flux correction was found to be predominantly active in the vicinity of wall boundaries. On the other hand, the difference could also be explained by the fact that the errors of the convective flow operator dominate at higher Reynolds numbers, causing the error terms, which are eliminated by the viscous flux correction, to be less important.

References

[1]Ekaterinaris, J. A., "High-order accurate, low numerical diffusion methods for aerodynamics," *Progress in Aerospace Sciences*, Vol. 41, No. 3-4, 2005, pp. 192–300.

[2]Cockburn, B. and Shu, C.-W., "TVB Runge-Kutta local projection discontinuous Galerkin finite element method for conservation laws. II. General framework," *Mathematics of Computation*, Vol. 52, No. 186, 1989, pp. 411–435.

[3]Cockburn, B., Lin, S.-Y., and Shu, C.-W., "TVB Runge-Kutta local projection discontinuous Galerkin finite element method for conservation laws III: One-dimensional systems," *Journal of Computational Physics*, Vol. 84, No. 1, 1989, pp. 90–113.

[4]Cockburn, B., Hou, S., and Shu, C.-W., "The Runge-Kutta local projection discontinuous Galerkin finite element method for conservation laws. IV. The multidimensional case," *Mathematics of Computation*, Vol. 54, No. 190, 1990, pp. 545–581.

[5]Cockburn, B. and Shu, C.-W., "The Runge-Kutta discontinuous Galerkin method for conservation laws V: Multidimensional systems," *Journal of Computational Physics*, Vol. 141, No. 2, 1998, pp. 199–224.

[6]Wang, Z. J., "Spectral (finite) volume method for conservation laws on unstructured grids: Basic formulation," *Journal of Computational Physics*, Vol. 178, No. 1, 2002, pp. 210–251.

[7]Wang, Z. J., Liu, Y., and Kwak, D., "Spectral (finite) volume method for conservation laws on unstructured grids II: Extension to two dimensional scalar equation," *Journal of Computational Physics*, Vol. 179, No. 2, 2002, pp. 665–697.

[8]Wang, Z. J. and Liu, Y., "Spectral (finite) volume method for conservation laws on unstructured grids III: One dimensional systems and partition optimization," *Journal of Scientific Computing*, Vol. 20, No. 1, 2004, pp. 137–157.

[9]Wang, Z. J., Zhang, L., and Liu, Y., "Spectral (finite) volume method for conservation laws on unstructured grids IV: Extension to two-dimensional systems," *Journal of Computational Physics*, Vol. 194, No. 2, 2004, pp. 716–741.

[10]Pont, G., Brenner, P., Cinnella, P., Maugars, B., and Robinet, J.-C., "Multiple-correction hybrid k-exact schemes for high-order compressible RANS-LES simulations on fully unstructured grids," *Journal of Computational Physics*, Vol. 350, 2017, pp. 45–83.

[11]Menasria, A., Brenner, P., Cinnella, P., and Pont, G., "Toward an improved wall treatment for multiple-correction k-exact schemes," *2018 Fluid Dynamics Conference, AIAA 2018-4164*, 2018.

[12]Setzwein, F., Ess, P., and Gerlinger, P., "An implicit high-order k-exact finite-volume approach on vertex-centered unstructured grids for incompressible flows," *Journal of Computational Physics*, Vol. 446, 2021, 110629.

[13]Setzwein, F., Ess, P., and Gerlinger, P., "Adaptive numerical dissipation control for high-order k-exact reconstruction schemes on vertex-centered unstructured grids using artificial neural networks," *Journal of Computational Physics*, Vol. 471, 2022, 111633.

[14]Chamarthi, A. S., Hoffmann, N., Bokor, S., Frankel, S. H., et al., "On the role of spectral properties of viscous flux discretization for flow simulations on marginally resolved grids," *Computers & Fluids*, Vol. 251, 2023, 105742.

[15]Setzwein, F., Ess, P., and Gerlinger, P., "High-order k-exact finite volume scheme for vertex-centered unstructured grids," *AIAA Scitech 2020 Forum, AIAA-2020-1785*, 2020.

[16]Setzwein, F., Spraul, M., Ess, P., and Gerlinger, P. M., "On the structure of correction matrices for a k-exact high-order finite-volume scheme on vertex-centered unstructured grids," *AIAA Scitech 2021 Forum, AIAA-2021-1548*, 2021.

[17]Barth, T. and Frederickson, P., "Higher order solution of the Euler equations on unstructured grids using quadratic reconstruction," *28th Aerospace Sciences Meeting, AIAA-90-0013*, 1990.

[18]Mathur, S. and Murthy, J., "A pressure-based method for unstructured meshes," *Numerical Heat Transfer*, Vol. 31, No. 2, 1997, pp. 195–215.

[19]Nishikawa, H., "A face-area-weighted 'centroid' formula for finite-volume method that improves skewness and convergence on triangular grids," *Journal of Computational Physics*, Vol. 401, 2020, 109001.

[20]Nishikawa, H., "A hyperbolic Poisson solver for tetrahedral grids," *Journal of Computational Physics*, 2020, 109358.

[21]Thomas, J. L., Diskin, B., and Nishikawa, H., "A critical study of agglomerated multigrid methods for diffusion on highly-stretched grids," *Computers & Fluids*, Vol. 41, No. 1, 2011, pp. 82–93.

[22]Muzaferija, S. and Gosman, D., "Finite-volume CFD procedure and adaptive error control strategy for grids of arbitrary topology," *Journal of Computational physics*, Vol. 138, No. 2, 1997, pp. 766–787.

[23]Demirdžić, I. and Muzaferija, S., "Numerical method for coupled fluid flow, heat transfer and stress analysis using unstructured moving meshes with cells of arbitrary topology," *Computer Methods in Applied Mechanics and Engineering*, Vol. 125, No. 1-4, 1995, pp. 235–255.

[24]Demirdžić, I., "On the discretization of the diffusion term in finite-volume continuum mechanics," *Numerical Heat Transfer, Part B: Fundamentals*, Vol. 68, No. 1, 2015, pp. 1–10.

[25]Jasak, H., *Error analysis and estimation for the finite volume method with applications to fluid flows.*, Ph.D. thesis, Imperial College London, 1996.

[26]Charest, M. R., Canfield, T. R., Morgan, N. R., Waltz, J., and Wohlbier, J. G., "A high-order vertex-based central ENO finite-volume scheme for three-dimensional compressible flows," *Computers & Fluids*, Vol. 114, 2015, pp. 172–192.

[27]Ollivier-Gooch, C. and Van Altena, M., "A high-order-accurate unstructured mesh finite-volume scheme for the advection-diffusion equation," *Journal of Computational Physics*, Vol. 181, No. 2, 2002, pp. 729–752.

[28]Khosla, P. and Rubin, S., "A diagonally dominant second-order accurate implicit scheme," *Computers & Fluids*, Vol. 2, No. 2, 1974, pp. 207–209.

[29]Schlichting, H. and Gersten, K., *Grenzschicht-Theorie*, Springer, 2006.

[30]Schäfer, M., Turek, S., Durst, F., Krause, E., and Rannacher, R., "Benchmark computations of laminar flow around a cylinder," *Flow Simulation with High-Performance Computers II*, Springer, 1996, pp. 547–566.

[31]Bassi, F., Crivellini, A., Di Pietro, D. A., and Rebay, S., "An implicit high-order discontinuous Galerkin method for steady and unsteady incompressible flows," *Computers & Fluids*, Vol. 36, No. 10, 2007, pp. 1529–1546.

[32]Tu, S. and Aliabadi, S., "Development of a hybrid finite volume/element solver for incompressible flows," *International Journal for Numerical Methods in Fluids*, Vol. 55, No. 2, 2007, pp. 177–203.

[33]Xie, B., Ii, S., Ikebata, A., and Xiao, F., "A multi-moment finite volume method for incompressible Navier-Stokes equations on unstructured grids: Volume-average/point-value formulation," *Journal of Computational Physics*, Vol. 277, 2014, pp. 138–162.

[34]Eggels, J., Unger, F., Weiss, M., Westerweel, J., Adrian, R. J., Friedrich, R., and Nieuwstadt, F., "Fully developed turbulent pipe flow: A comparison between direct numerical simulation and experiment," *Journal of Fluid Mechanics*, Vol. 268, 1994, pp. 175–210.

[35]Fukagata, K. and Kasagi, N., "Highly energy-conservative finite difference method for the cylindrical coordinate system," *Journal of Computational Physics*, Vol. 181, No. 2, 2002, pp. 478–498.

[36]Ducros, F., Nicoud, F., and Poinsot, T., "Wall-adapting local eddy-viscosity models for simulations in complex geometries," *Numerical Methods for Fluid Dynamics VI*, 1998, pp. 293–299.

[37]Nicoud, F. and Ducros, F., "Subgrid-scale stress modelling based on the square of the velocity gradient tensor," *Flow, Turbulence and Combustion*, Vol. 62, No. 3, 1999, pp. 183–200.